2016-12

# Skill assessment of HF radar-derived products for Lagrangian simulations in the Bay of Biscay

Solabarrieta, Lohitzune; Forlov, Sergey; Cook, Mike; Paduan, Jeff; Rubio, Anna; González, Manuel; Mader, Julien; Charria, Guillaume

American Meteorological Society

Lohitzune Solabarrieta, et al, "Skill assessment of HF radar-derived products for Langrangian simulations in the Bay of Biscay," Journal of Atmospheric and Oceanic Technology, v. 33, (December 2016), pp.2585-2597.
https://hdl.handle.net/10945/51736

# Skill Assessment of HF Radar–Derived Products for Lagrangian Simulations in the Bay of Biscay

LOHITZUNE SOLABARRIETA[a]

*Marine Research Unit, AZTI-Tecnalia, Pasaia, Spain*

SERGEY FROLOV

*University Corporation for Atmospheric Research, Boulder, Colorado, and Naval Research Laboratory, Monterey, California*

MIKE COOK AND JEFF PADUAN

*Naval Postgraduate School, Monterey, California*

ANNA RUBIO, MANUEL GONZÁLEZ, AND JULIEN MADER

*Marine Research Unit, AZTI-Tecnalia, Pasaia, Spain*

GUILLAUME CHARRIA

*Laboratoire d'Océanographie Physique et Spatiale, Plouzané, France*

(Manuscript received 24 February 2016, in final form 17 June 2016)

ABSTRACT

Since January 2009, two long-range high-frequency (HF) radar systems have been collecting hourly high-spatial-resolution surface current data in the southeastern corner of the Bay of Biscay. The temporal resolution of the HF radar surface currents permits simulating drifter trajectories with the same time step as that of real drifters deployed in the region in 2009. The main goal of this work is to compare real drifter trajectories with trajectories computed from HF radar currents obtained using different methods, including forecast currents. Open-boundary modal analysis (OMA) is applied to the radar radial velocities and then a linear autoregressive model on the empirical orthogonal function (EOF) decomposition of an historical data series is used to forecast OMA currents. Additionally, the accuracy of the forecast method in terms of the spatial and temporal distribution of the Lagrangian distances between observations and forecasts is investigated for a 4-yr period (2009–12). The skills of the different HF radar products are evaluated within a 48-h window. The mean distances between real trajectories and their radar-derived counterparts range from 4 to 5 km for real-time and forecast currents after 12 hours of simulations. The forecast model improves persistence (i.e., the simulations obtained by using the last available OMA fields as a constant variable) after 6 hours of simulation and improves the estimation of trajectories up to 28% after 48 hours. The performance of the forecast is observed to be variable in space and time, related to the different ocean processes governing the local ocean circulation.

## 1. Introduction

Since January 2009, two long-range high-frequency (HF) radar systems have been collecting hourly high-spatial-resolution surface current data (~5 km) in the southeastern corner of the Bay of Biscay. The study area is situated between 43°30′–44°40′N and 1°–3°30′W (Fig. 1), off the coast of the Basque Country, Spain,

AZTI Contribution Number 772.

[a] Current affiliation: DeustoTech Energy, Bilbo, Spain.

*Corresponding author address*: Lohitzune Solabarrieta, Marine Research Unit, AZTI-Tecnalia, Herrera Kaia, Portualdea z/g, 20110 Pasaia, Gipuzkoa, Spain.
E-mail: lohisola@hotmail.com

DOI: 10.1175/JTECH-D-16-0045.1

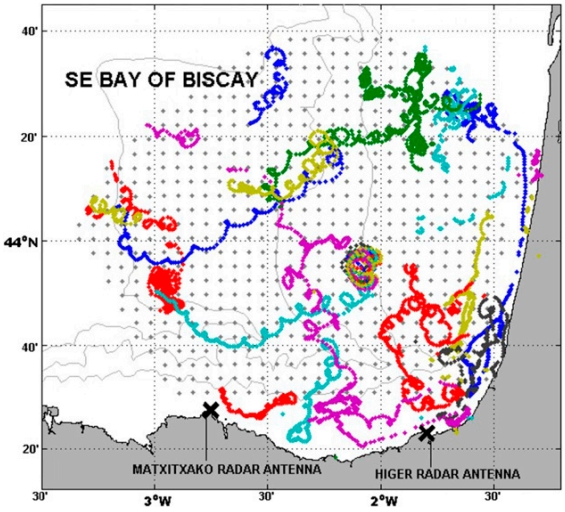


FIG. 1. Study area. Crosses show the position of the HF radar antennas at Cape Higuer and Cape Machichaco. Gray points correspond to the nodes of the grid used to build radar-derived total current fields, and gray lines denote topographic contours (isobaths: 200, 1000, 2000 m). Colored lines show the trajectories of the 20 surface drifters used in the analyses.

and southwestern France. The coast is oriented roughly east–west along the Spanish coast and north–south along the French coast, and this discontinuity delineates the main bathymetric features of the study region. Figure 1 shows that the French shelf becomes progressively wider to the north, while the Spanish shelf is much narrower with a constant width (30–40 km) over the entire study area.

The primary circulation pattern in the southeastern corner of the Bay of Biscay is cyclonic in winter and anticyclonic in summer. The analysis of low-pass-filtered currents shows that a key component of this variability is associated with the surface signature of the slope current [Iberian Poleward Current (IPC)], which is more intense over the upper part of the slope (Solabarrieta et al. 2014). In winter, the IPC flows eastward along the Spanish coast and northward along the French coast, affecting the upper water column from the surface to 300-m depth (Le Cann and Serpette 2009) and is associated with warm surface waters along the northern Spanish slope (Pingree and Le Cann 1990). From the joint analysis of ADCP, HF radar, and North Atlantic Oscillation (NAO) index databases, eastward (northward) surface currents of 70 cm $s^{-1}$ were observed along the Spanish (French) slope, related to the winter IPC (Solabarrieta et al. 2014). In summer, the circulation over the slope is reversed; that is, it presents a westward (southward) flow over the Spanish (French) slope, with intensities 3 times weaker (~10–20 cm $s^{-1}$) than those observed in winter (Solabarrieta et al. 2014). Because of the stronger stratification of the water column, the vertical gradients of the horizontal currents in summer show a higher vertical shear than in winter (Rubio et al. 2013a).

In addition to the marked seasonality of the shelf/slope current regime, several authors have described the presence of mesoscale cyclonic and anticyclonic eddies in the area. These eddies are generated most frequently during winter by the interaction of the IPC with the abrupt bathymetry (Pingree and Le Cann 1990, 1992a,b; van Aken 2002; Le Cann and Serpette 2009). Recently, Rubio et al. (2013b) provided evidence of the presence of coherent mesoscale structures within the HF radar footprint area and of their potential effect on local transport paths.

Overlaid to the density-driven slope circulation, wind-induced currents are the main drivers of the surface ocean circulation in the HF radar footprint area and are observed in a wide range of time scales, from seasonal to high frequency (Fontán et al. 2013; Fontán and Cornuelle 2015; Solabarrieta et al. 2015; Kersalé et al. 2016). During autumn and winter, southwestern winds dominate and generate northward and eastward drift over the shelf. The wind regime changes to the northeast during spring, when it causes sea currents toward the west-southwest along the Spanish coast. The summer situation is similar to that of spring, but the weakness of the winds and the greater variability of the direction of the general drift make currents more uncertain (González et al. 2004; Solabarrieta et al. 2015). Solabarrieta et al. (2015) used the *k*-means clustering technique to characterize the main ocean surface circulation patterns in the study area, at scales from several days to interannual, showing the high variability in terms of surface currents and wind–current interactions.

At shorter time scales, the variability is dominated by inertial oscillations and tides (mainly semidiurnal), although energy contents around the main tidal peaks are lower than in other areas of the bay (Le Cann 1990). Indeed, values observed for $M_2$, which is the most energetic component, are below 10 cm $s^{-1}$ (Le Cann 1990; Rubio et al. 2013a). The contribution of inertial oscillations to the shear-induced vertical mixing over the slope was discussed by Rubio et al. (2013a). From HF radar data, the distribution of kinetic energy around the inertial band and its contribution to the total variability was observed to be highly variable in time and space; inertial oscillations are seasonally modulated and intensified in summer in the central part of the study area (Rubio et al. 2011; Solabarrieta et al. 2014). Surface inertial currents over 15 cm $s^{-1}$ have been observed over the slope of the study area during stratified conditions (Rubio et al. 2011).

An area characterized by such complex circulation patterns and where relevant human activities linked to marine resources concentrate (artisanal and commercial fishing, tourism, industry, increasing offshore aquaculture and marine renewables, etc.) represents a particular challenge for the accurate monitoring and forecasting of surface transport patterns. In this context, the main goal of this paper is to compare real drifter trajectories with simulated trajectories computed from HF radar–derived currents using different processing methodologies, including forecast currents. The temporal resolution of the HF radar–derived surface currents (hourly data) enables the simulation of surface drifter trajectories with the same time step as that of real drifters that were deployed in the region during several campaigns in 2009 (Charria et al. 2013). Additionally, the performances of the forecast method used here are investigated, using a longer period of available HF radar data, in terms of the spatial and temporal distribution of Lagrangian distances between radar-derived and forecast trajectories.

## 2. Data and methods

### a. Data

A main component of the Basque Country's in situ operational oceanography observational network includes two long-range CODAR Ocean Sensors SeaSonde HF radar systems, owned by the Directorate of Emergency Attention and Meteorology of the Basque government's Security Department. The radar antennas are located at Cape Machichaco and Cape Higuer (Fig. 1) and emit at a central frequency of 4.5 MHz and a 40-kHz bandwidth. The range coverage of radial data is close to 180 km, with 5-km radial resolution.

Hourly HF radar data within the period 2009–12 are used in this study. Basque HF radar validation exercises with suitable results have been performed previously by several authors and they can be checked in Solabarrieta et al. (2014) and Rubio et al. (2011). HF radar technology is more detailed in Paduan and Rosenfeld (1996), Paduan and Graber (1997), and Paduan and Washburn (2013).

From April to September 2009, different campaigns launched several drifter buoys within the Bay of Biscay and 20 of them were used in this study. More information about the buoys can be obtained in Charria et al. (2013). All the buoys had similar characteristics, with a surface float linked to a long (~10 m long × ~1 m wide) holey-sock drogue by a thin (~5 mm) cable and centered at 15-m depth. The position was transferred by an Argos localization system every hour. The lifetimes of the 20 real buoys used in this study ranged from several days to more than three months. The spatial distribution of the drifters is plotted in Fig. 1 and the temporal distribution these data within the period April–September 2009, and conditioned to the availability of HF radar data, can be checked in Solabarrieta et al. (2014) (Fig. 2). The drifters covered distances from a few kilometers up to 443 km, with speeds between 6.78 and 37.95 cm $s^{-1}$ (with a mean value of 18.69 cm $s^{-1}$ and a standard deviation of 9.08 cm $s^{-1}$). As the buoys were linked to a drogue centered at 15-m depth, it is important to highlight that the deployments took place during mostly stratified months. The same drifter dataset was used for Eulerian comparisons with HF radar velocities in Solabarrieta et al. (2014). The differences observed between drifter-derived velocities and HF radar within the HF radar footprint area showed RMS values of approximately 13 cm $s^{-1}$. These values were in agreement with those obtained through a comparison with current data at 12 m measured by the ADCPs located in two moored buoys over the slope during stratified conditions. The differences observed between HF radar data and moored ADCP velocities in stratified conditions for a longer time series (2009–11) were similar and higher than those observed in well-mixed periods. As already discussed in Solabarrieta et al. (2014), when analyzing the comparisons between the drifters used here and the HF radar data, it has to be kept in mind that the effective averaging depth for surface current measurements by HF radars has been estimated as 5%–16% of the wavelength of the backscattering surface waves (Barrick 1977; Fernández et al. 1996; Stewart and Joy 1974). For the Basque Country system (4.5 MHz), the measurements made are expected to integrate currents vertically within the first ~2 m of the water column. Since the nominal depth of the available drifter trajectories ranges from 10 to 20 m and most of the trajectories are obtained during stratified conditions, part of the differences in the drift between real and simulated trajectories can be related to the vertical shear of the current [detailed in Fig. 5 in Solabarrieta et al. (2014)]. Moreover, it can also be expected that horizontal current shear also contribute to the differences observed between measurements (drifters measure currents at punctual locations and discrete times, while HF radar velocities are running averages over three hours and several square kilometers).

### b. Methods

The received signal, an averaged Doppler backscatter spectrum received every 20 min, was processed to radial current using the Multiple Signal Classification (MUSIC) algorithm (Schmidt 1986) as applied by the manufacturer, CODAR Ocean Sensors. The radial velocity fields obtained were stored hourly after applying a

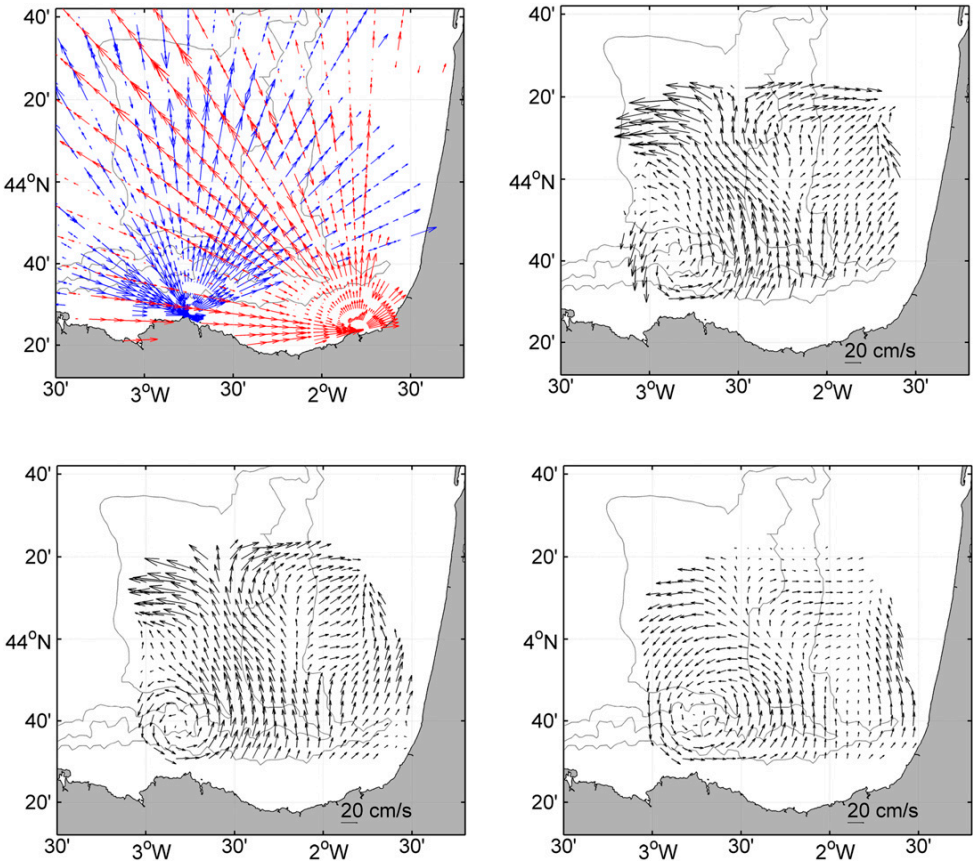


FIG. 2. Snapshots of the surface currents at 1300 UTC 13 Feb 2011, for (top left) radial currents from the two radar sites; (top right) total currents, generated from radial currents; (bottom left) currents generated by OMA analysis; and (bottom right) 24-h forecast currents for the same date (i.e., calculated starting at 1300 UTC 12 Feb to 1300 UTC 13 Feb).

running-average smoother (centered on a 3-h window). For this work, the radial velocities were quality controlled and converted to total fields, using the HFR_Progs MATLAB package (https://cencalarchive.org/ProgsRealTime/), based on Gurgel (1994) and Lipa and Barrick (1983, see section 2.6). To obtain total currents gridded into a 5-km-resolution regular orthogonal mesh (see Fig. 1), a least-mean-square algorithm (spatial interpolation radius of 10 km) was applied. Both the spatial resolution for the total grid and the interpolation radius were chosen to resolve the smallest spatial scales within the limits of the resolution of the radial data.

Using the same grid, radial velocities are processed with HFR_Progs to generate open-boundary modal analysis (OMA)-derived currents (OMA currents; Kaplan and Lekien 2007). OMA is a robust methodology that permits generating gap-filled total currents from radials. OMA can also be used to produce total currents when the radial data coverage is not complete or a radial file is missing, and also to increase the coverage in the baseline area. To be able to make a comparison between OMA and total currents, for our study we use OMA currents only in the time steps where the two radial files exist and in the areas where the geometric dilution of precision (GDOP) quality criteria errors are under established thresholds (see Solabarrieta et al. 2014). In this study a total of 85 physical modes built setting a minimum spatial scale of 20 km were used to generate the velocity fields.

Finally, to forecast OMA interpolated currents, we used the linear autoregressive models described in Frolov et al. (2012). In short, the empirical orthogonal function (EOF) analysis was first applied to the OMA gridded fields and the 50 leading EOF modes were retained. For the time series of these leading EOF modes, a vector autoregressive model was constructed and then used for prediction. Because of the combination of the EOF preprocessing and the time embedding

in the autoregressive model (up to 48 hours in the past), the forecast model is able to simultaneously learn both the high-frequency signal (tidal and inertial) and the basinwide modes of the circulation.

An example of the fields obtained, using the previously described processing methods for 1300 UTC 13 February 2011, is provided in Fig. 2. In this example, the radial coverage is not optimal for the system with reduced ranges for the Higer antenna at bearing angles (i.e., the direction from the radar site location to the radial grid point; bearing 90° means that the radial grid point is located north of the radar site location) between 80° and 90° and reduced ranges for the Matxitxako antenna from 0° to 30°. As a result the total velocities at the southeastern corner of the footprint area cannot be obtained using the least-mean-square algorithm (Fig. 2, top right). The OMA reconstruction is able to fill this spatial gap and results in a current field very similar to the total field. The 24-h forecast in Fig. 2 (bottom right) is calculated from the OMA field of 1300 UTC 12 February 2011using the forecast model. In this example, the resulting field for 13 February shows similar structures to the OMA field for the same date and time but weaker intensities and spatially smoothed velocities.

To simulate trajectories in the differently processed HF radar current fields, a new version (adapted to 2D fields) of the Lagrangian particle-tracking model (LPTM) developed by Ferrer et al. (2009) for 3D numerical simulations of currents was used here. The method for the particle movement in this LPTM is based upon the fourth-order Runge–Kutta scheme (Benson 1992) and permits the calculation of multiple trajectories at a low computational cost. Trajectories obtained using as a constant variable the latest available OMA current field at the time simulations start (persistence currents) are also included in the comparisons. This enables the estimation of the variability of the current field during the simulation period and offers a reference for evaluating the benefits of using forecast currents instead of persistence fields for operational purposes.

For the comparison with the in situ trajectories, and in order to have more than one comparison trajectory for each real drifter track (20 real drifters in total), one trajectory was generated every 6 hours starting along the corresponding positions of each real track, obtaining more than 4500 starting points to simulate trajectories for comparison exercises. Each particle was then advected during 48 hours using the LPTM and the currents of the differently processed datasets. In this way, the number of comparison tracks increased substantially (see Fig. 3, top and middle, as an example of the comparison track obtained for one particle). For the analysis of the forecast model performances in a longer period, trajectories have

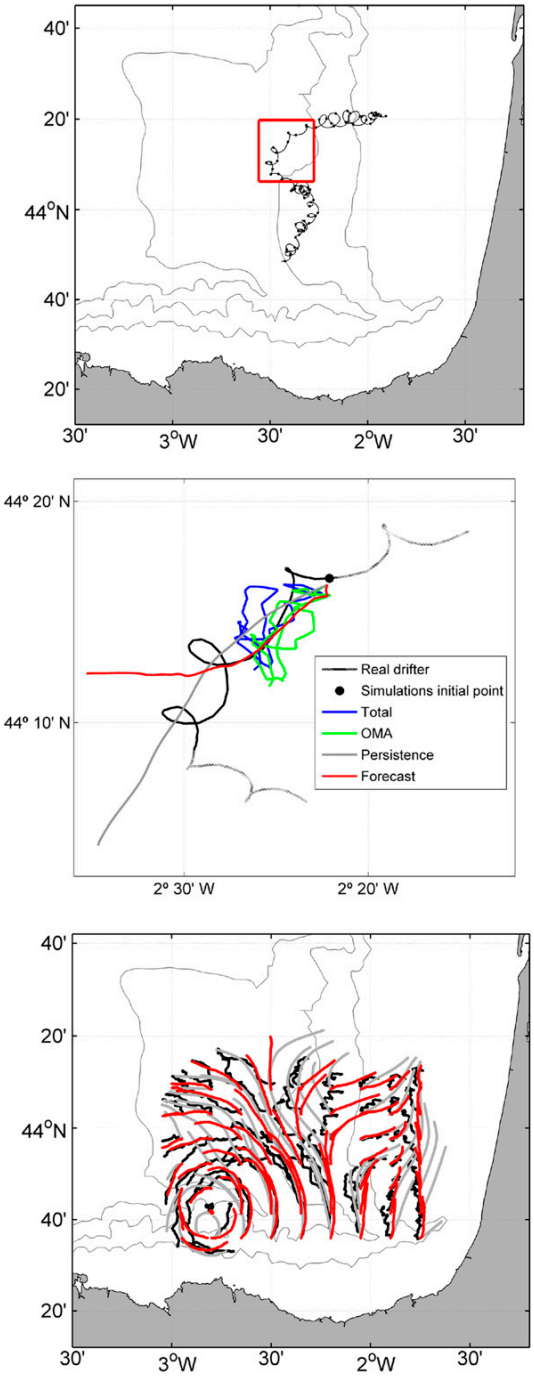


FIG. 3. (top) Example of real drifter trajectory (black line) and starting positions for Lagrangian simulations (black dots). (middle) Real drifter [zoomed-in view of the trajectory in the red square area in (top)] and simulated trajectories during 48 hours using various HF radar–derived current fields (48-h real drifter track used as a reference for comparisons is shown in solid black). (bottom) Example of 48-h trajectories from different HF radar–derived products starting at 1300 UTC 13 Feb 2011: OMA (black), persistence (gray), and forecast fields (red).

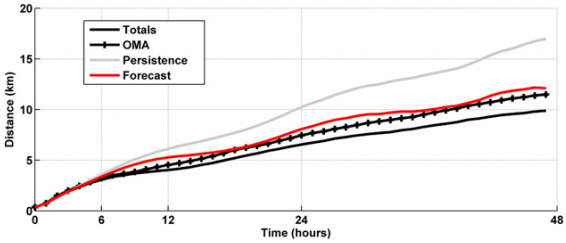


FIG. 4. Time evolution of the mean separation distance between real drifter trajectories and their simulated counterparts using total, OMA, and forecast currents.

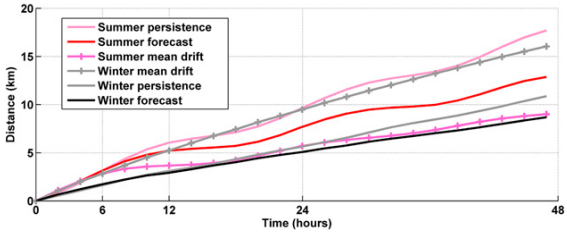


FIG. 5. Time evolution of the mean separation distance between trajectories (solid lines) generated using persistence currents and forecast currents for summer and winter periods. Lines with markers show the mean drift velocities of all the trajectories generated in OMA fields for each period (i.e., the separation from the initial positions with time).

been generated every hour using trajectories launched in a regular 9 × 7 grid, covering the study area with regular node distances of 0.15° × 0.09° (Fig. 3, bottom). In all cases, the trajectories of the particles going out of the HF radar footprint at any time of the simulation are disregarded. As can be observed in this example, the trajectories generated using persistence fields are quite similar to those generated using time-evolving OMA currents and suggests that the current pattern observed at the initial time step (Fig. 2, bottom left) persists during the following 48 hours. Thus, the differences between persistence and forecast are weak in most of the domain. The strongest differences are observed at the eastern part of the domain, where the trajectories obtained using the forecast show smaller differences with their OMA counterparts. Persistence fields generate smooth trajectories that tend to overestimate the net displacement of the particles in the OMA fields.

The differences between real and simulated trajectories have been estimated using the separation distance average ($\sqrt{x^2+y^2}$) between real and simulated trajectories. The mean separation distances obtained using all of the comparison pairs (real trajectories vs simulated trajectories with differently processed current fields) have been plotted against time up to 48 hours (Figs. 4 and 5). The spatial distribution of longitude and latitude distances between real and simulated trajectories has been also analyzed in order to detect any anisotropy in the differences between them.

Then, the probability density distribution of the distances between real and simulated trajectories after 6, 12, 24, and 48 hours were computed. To have a robust quantification of the main differences between trajectories, a lognormal function was adjusted to the distributions of distances. Then, the lognormal probability density function can be obtained using

$$y = f(x \mid \mu, \sigma) = \frac{1}{x\sigma\sqrt{2\pi}} e^{(\ln x - \mu)^2/2\sigma^2},$$

where $\mu$ and $\sigma$ are the mean and the standard deviation (std dev), respectively, of the lognormal distribution for the fitted data. The mean and standard deviation of each fit function, and the values of these two parameters corresponding to the lower and upper confidence bounds within a 95% confidence interval, are summarized in Tables 1 and 2. Finally, the benefits of using forecast currents instead of persistence currents are calculated as a dimensionless percent value using

$$100 \times \frac{D_p - D_f}{D_p},$$

where $D_p$ is the mean distance obtained using persistence and $D_f$ is the mean distance obtained using the forecast model (Table 3).

## 3. Comparison between HF radar–derived and real trajectories

The average separation velocity (km h$^{-1}$) of the studied real drifters is 0.75 km h$^{-1}$. The cumulative separation distances between the real and the simulated trajectories (Fig. 4) show a separation rate (i.e., the increase with time of the mean distances between trajectories) of 0.5 km h$^{-1}$, during the first six hours of simulation. No difference in performance between the differently processed HF radar data is observed at shorter time lags (Fig. 4). After six hours of simulation, the differences start to be visible, with the total and OMA currents presenting the lowest separation ratios, of 0.27 and 0.37 km h$^{-1}$, respectively. The trajectories obtained using forecast currents show a separation ratio similar to the OMA trajectories (0.33 km h$^{-1}$), while the trajectories obtained assuming the persistence of the initial OMA field show

TABLE 1. Statistical parameters for lognormal distributions of distances between real and simulated trajectories in Fig. 5, after 6, 12, 24, and 48 hours of simulations with total, OMA, persistence, and forecast currents. Values corresponding to the distributions within the 95th percentile are given in square brackets.

| | Totals | | OMA | | Persistence | | Forecast | |
|---|---|---|---|---|---|---|---|---|
| Time (h) | Mean | Std dev | Mean | Std dev | Mean | SD | Mean | Std dev |
| 6 | 2.85 | 2.01 | 2.91 | 2.14 | 3.15 | 2.51 | 2.98 | 2.24 |
| | [2.61, 3.14] | [1.69, 2.42] | [2.65, 3.21] | [1.081, 2.58] | [2.85, 3.49] | [2.09, 3.05] | [2.69, 3.34] | [1.85, 2.77] |
| 12 | 4.07 | 3.19 | 4.47 | 3.61 | 6.05 | 5.08 | 5.29 | 4.12 |
| | [3.68, 4.54] | [2.65, 3.91] | [4.01, 4.96] | [2.99, 4.43] | [5.44, 6.77] | [4.20, 6.24] | [4.74, 5.95] | [3.37, 5.14] |
| 24 | 6.59 | 5.25 | 7.42 | 6.13 | 10.23 | 9.47 | 7.93 | 6.36 |
| | [5.92, 7.38] | [4.32, 6.49] | [6.66, 8.33] | [5.03, 7.59] | [9.08, 11.64] | [7.68, 11.93] | [7.06, 9.00] | [5.13, 8.05] |
| 48 | 10.29 | 7.51 | 12.16 | 11.16 | 17.65 | 14.74 | 12.59 | 10.87 |
| | [9.28, 11.51] | [6.17, 9.31] | [10.68, 14.01] | [8.88, 14.37] | [15.7, 20.04] | [11.92, 18.62] | [10.98, 14.65] | [8.50, 14.31] |

higher errors (with a separation ratio of 0.4 km $h^{-1}$). At the end of the simulation (48 hours), the trajectories obtained using OMA and forecast currents present separation distances over 10 km with respect to the real ones, while those obtained using persistence currents show separation distances over 15 km.

The values obtained by adjusting a lognormal curve to the probability density distributions of the distances between all the trajectories at 6, 12, 24 and 48 hours are shown in Table 1. After six hours, the separation distance from real drifters is around 2.85 km for total currents and 2.98 km for forecast currents, while these values increase up to 6.59 and 7.93 km, respectively, after 24 hours of simulation. The separation distances obtained using OMA currents are between these values. This means that the inaccuracies in the OMA solution for total currents are contributing to the differences observed using the forecast model and the persistence fields, both obtained using OMA currents. Persistence shows separation values with respect to real trajectories over 10 km after 24 hours of simulation. The examination of the zonal and meridional distances with time does not show any anisotropy (not shown).

TABLE 2. Statistical parameters for lognormal distributions of distances (a) between OMA and persistence trajectories and (b) between OMA and forecast trajectories, after 6, 12, 24, and 48 hours of simulation. Values corresponding to the distributions within the 95th percentile are given in square brackets.

| | | (a) Persistence | | (b) Forecast | |
|---|---|---|---|---|---|
| | Time (h) | Mean | Std dev | Mean | Std dev |
| All periods | 6 | 2.68 | 2.27 | 2.69 | 2.21 |
| | | [2.67, 2.7] | [2.25, 2.29] | [2.68, 2.71] | [2.19, 2.23] |
| | 12 | 5.29 | 4.62 | 4.54 | 3.84 |
| | | [5.26, 5.32] | [4.58, 4.67] | [4.51, 4.57] | [3.8, 3.88] |
| | 24 | 8.68 | 7.32 | 6.87 | 5.54 |
| | | [8.63, 8.73] | [7.25, 7.4] | [6.83, 6.91] | [5.49,5.6] |
| | 48 | 16.2 | 13.55 | 11.62 | 9.35 |
| | | [16.11, 16.29] | [13.42, 13.69] | [11.56, 11.68] | [9.26, 9.44] |
| Summer | 6 | 3.25 | 2.55 | 3.29 | 2.59 |
| | | [3.21, 3.28] | [2.5, 2.6] | [3.25, 3.32] | [2.54, 2.63] |
| | 12 | 6.27 | 4.86 | 5.42 | 4.29 |
| | | [6.2, 6.33] | [4.77, 4.95] | [5.37, 5.48] | [4.21, 4.37] |
| | 24 | 10.05 | 7.88 | 7.95 | 5.94 |
| | | [9.95, 10.16] | [7.74, 8.03] | [7.88, 8.03] | [5.84, 6.05] |
| | 48 | 18.36 | 13.83 | 13.37 | 10.14 |
| | | [18.18, 18.54] | [13.59, 14.09] | [13.24, 13.5] | [9.96, 10.33] |
| Winter | 6 | 1.69 | 1.38 | 1.8 | 1.41 |
| | | [1.67, 1.71] | [1.35, 1.41] | [1.78, 1.82] | [1.38, 1.44] |
| | 12 | 3.21 | 2.55 | 3.08 | 2.56 |
| | | [3.18, 3.25] | [2.49, 2.6] | [3.04, 3.12] | [2.51, 2.62] |
| | 24 | 5.8 | 4.6 | 5.33 | 4.42 |
| | | [5.73, 5.87] | [4.5, 4.7] | [5.27, 5.4] | [4.32, 4.52] |
| | 48 | 11.25 | 9.28 | 9.01 | 7.78 |
| | | [11.11, 11.39] | [9.08, 9.49] | [8.89, 9.12] | [7.61, 7.96] |

TABLE 3. Benefit of STP compared to persistence for 6-, 12-, 24-, and 48-h time lags in the different study periods: 2009 (using real trajectories), summer (for summer months in the period 2009–12, using OMA-derived trajectories) and winter (for winter months in the period 2009–12, using OMA-derived trajectories). Benefit in percent is calculated as detailed in section 2b.

| Time (h) | 2009 | 2009–12 | Summer | Winter |
|---|---|---|---|---|
| 12 | 12.5% | 15.1% | 13.6% | 4% |
| 24 | 22.5% | 20.9% | 20.9% | 8% |
| 48 | 28.6% | 28.4% | 27.2% | 19.9% |

## 4. Analysis of the forecast model spatiotemporal performances

The cumulative separation distances between simulated trajectories using OMA and those obtained using persistence and forecast currents are examined for two different seasons for the period 2009–12 (Fig. 5). The separation between the simulated trajectories using OMA and the ones using forecast and persistence currents are similar during the first six hours of simulation (around 0.44 km $h^{-1}$). The separation rates vary seasonally from 0.54 km $h^{-1}$ in summer to 0.3 km $h^{-1}$ in winter. In both cases, and for both datasets, the separation rates for time horizons of 24–48 hours are lower: around 0.41 and 0.33 km $h^{-1}$ for persistence and forecast, respectively, in summer, and 0.24 and 0.22 km $h^{-1}$ for persistence and forecast, respectively, in winter. A higher rate of separation between persistence and OMA trajectories indicates a higher spatial–temporal variability in summer currents, despite the fact that they are expected to be much less intense than the wintertime currents. A higher rate of separation between persistence and forecast trajectories suggests that the skills of the forecast model to predict summer (much more variable) current fields are lower. It is worth noting that the skills of the forecast model in summer are lower than those shown by persistence trajectories in winter. However, Fig. 4 suggests that the benefits of the forecast relative to persistence currents are higher in summer than in winter. At the end of the simulation (48 hours), the trajectories obtained using forecast currents present distances around 7.5 and 10 km in winter and summer, respectively.

The values obtained by adjusting a lognormal curve to the probability density distributions of the distances between all the simulated trajectories for the different seasons at 6, 12, 24, and 48 hours are shown in Table 2. After six hours, the mean separation distance for forecast currents is around 3.29 and 1.8 km in summer and winter, respectively, while these values after 24 hours of simulation increase to 7.95 and 5.33 km in summer and winter, respectively. Persistence shows separation values with respect to OMA trajectories of 10 km in summer and 5.8 km in winter after 24 hours of simulation. As for the comparison with real trajectories, no anisotropy was found in the distributions of the zonal and meridional distances at any simulation time (not shown).

When the results are analyzed, spatially significant differences in the performance of the forecast model can also be observed, which are in agreement with the spatial variability of the persistence. In summer (Fig. 6), the area where trajectories are reproduced with the lowest skills is the northwestern part of the domain, with the distances lower in the southern part of the domain and along the shelf and slope. The differences between OMA trajectories and those in persistence and forecast are the highest and can reach values in the northwestern part of the domain, over 12 and 20 km, at 24 and 48 hours, respectively. In summer the differences between trajectories using OMA currents and persistence are high (>20 km) in almost all the domain after 48 hours, while these are still under 12 km over the slope area for the forecast currents (Fig. 6). The benefits of forecast in summer can be seen mostly in this area of low persistence.

In winter (Fig. 7), an area with increased differences between OMA and persistence and forecasts located in the northwestern part of the domain can be still observed, but it is much more reduced spatially. High differences between trajectories are instead observed along the shelf/slope. Globally, absolute differences are lower in winter than in summer in the whole domain. Values in the slope area over 6.5 and 12.7 km can be observed for persistence at 24 and 48 hours, respectively (Fig. 7). These are reduced by the forecast to values over 5.5 and 10 km at 24 and 48 hours, respectively.

## 5. Discussion

The skills of different HF radar–derived products to reproduce observed trajectories have been analyzed using real drifter data available within the radar footprint area in 2009. Further analyses have been performed using the complete HF radar dataset available for the study area in order to investigate the temporal and spatial variability of the performances of the forecast products.

The differences between real trajectories and simulated trajectories obtained using HF radar total currents show values between 2.85 and 6.59 km after 6 and 24 hours of simulation, respectively. Similar to what was discussed in Solabarrieta et al. (2014) and Rubio et al. (2011) in terms of Eulerian differences, different aspects can contribute to the differences between the real and HF radar–derived trajectories obtained here. Since

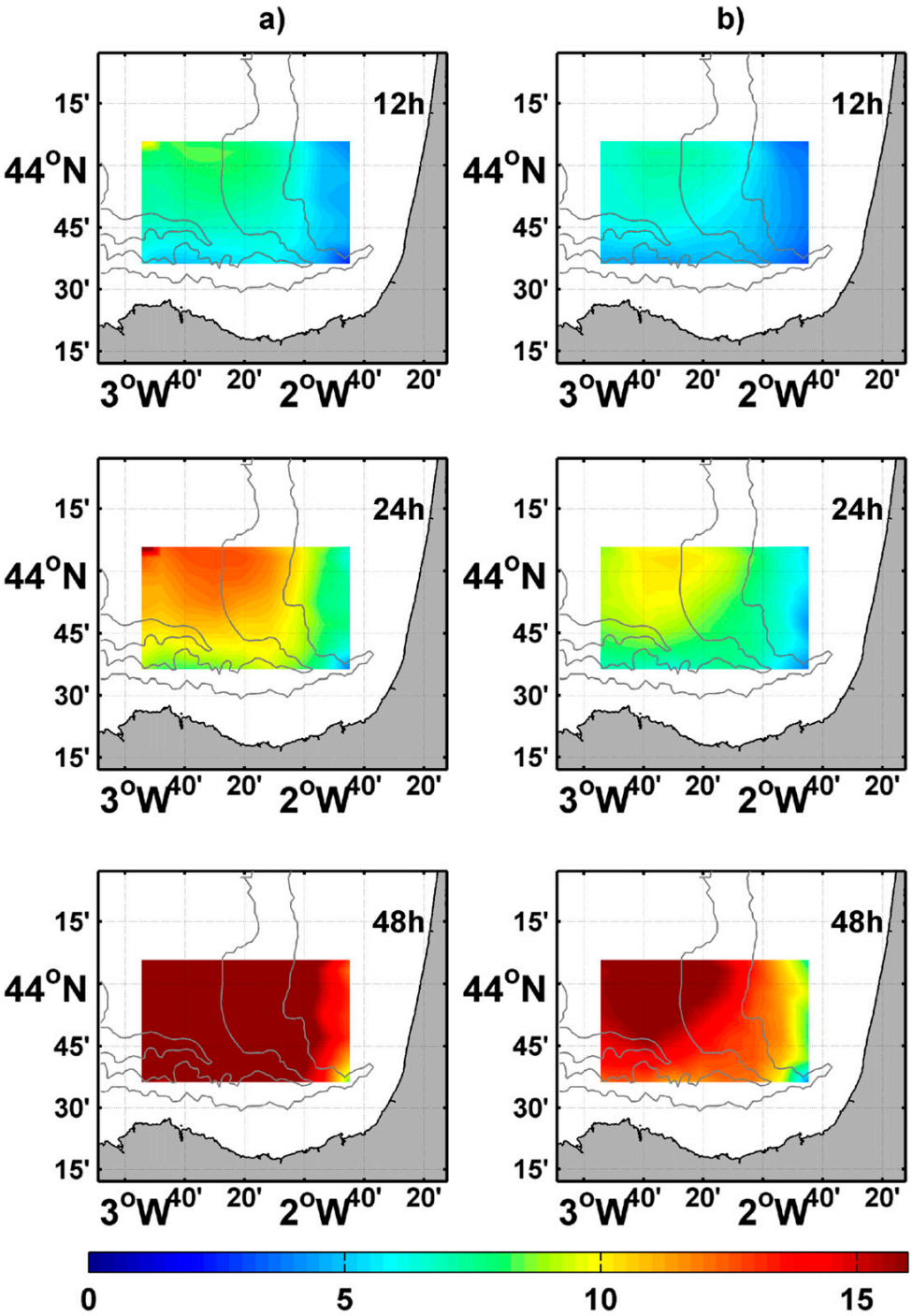


FIG. 6. Spatial distribution of errors (separation distances in km) in summer for (a) persistence and (b) forecast data products using trajectories from OMA currents as reference, in function of the initial position of the particle used for the computation of the trajectories.

vertical and horizontal current shears can be expected to be high in the period when the drifters were deployed, it can be expected that the skills of the HF radar–derived total velocities to reproduce real trajectories will be improved for periods with greater homogeneity in the upper part of the water column. These differences can also be expected to be reduced by the use of surface drifters [e.g., Coastal Ocean Dynamics Experiment (CODE) drifters; see Berta et al. 2014], with an equivalent integration depth to that of the Basque Country HF radar system (~1 m), or by the use of drifter spatial clusters, as discussed in Ohlmann et al. (2007).

The quality of OMA reconstruction has also been proved by our results, since in the area covered by two radials where total velocities reconstruction is possible, this solution does significantly degrade the estimations. Higher inaccuracies due to the reconstruction from radials to totals can be expected near the baseline area and also in periods of short temporal (few hours) radial data gaps when OMA can still be used to retrieve total currents. The use of OMA velocities when only one antenna is working and the analysis of the results using these velocities are out of the scope of this paper. Although this possibility offers velocity fields with fewer gaps, which is beneficial for operational use, it is also expected to add to the uncertainties.

In terms of forecast currents, the comparisons between projected and real trajectories lead to mean differences under 3 km at six hours (i.e., adding significant error to the estimation provided by total currents) and under 8 km within a forecast horizon of 24 hours. During all of the simulation periods, the forecasted trajectories represent improvements over the estimations provided by persistence fields (i.e., considering the last available OMA field remains stationary for the entire simulation period). The comparison results are similar and agree with those obtained by Ullman et al. (2006) and Kohut et al. (2012), using HF radar data and drifters. The benefit of the forecast method with respect to persistence is 12.5% after 12 hours of simulations, and it grows to 28.6% after 48 hours (Table 3). These results are similar to the benefits of forecast trajectories relative to persistence-based trajectories obtained using all available HF radar observations from 2009 to 2012, which show benefits around 15.0% after 12 hours and 28.4% after 48 hours.

When analyzing projected trajectories based on the forecast model and persistence for the period 2009–12, spatial and seasonal variability of the performances are observed. Seasonally, the benefits of forecast relative to persistence range from 4% to 13.6% after 12 hours and from 19.9% to 27.26% after 48 hours, with the highest benefits observed during summer (Table 3). Indeed, in summer the errors of the forecast are higher in absolute values but since the surface current fields are more variable (less persistent), the relative benefits of employing the forecast model are higher. If we compute the average distances covered by the drifters simulated with OMA fields (i.e., the separation with time along each trajectory from its starting positions), a dispersion rate of 0.2 km $h^{-1}$ is observed in summer. By comparison, the separation rate between OMA trajectories and forecast trajectories is around 0.33 km $h^{-1}$. Hence, we conclude that the skill of the forecast product in summer needs to be improved. The winter situation is slightly different. Since there is a more persistent current regime, the estimation of projected trajectories can, in general, be done with lower errors. At the same time, the benefits of using forecast currents instead of persistence are also lower. The average distance covered by winter drifters in time gives a dispersion rate of 0.36 km $h^{-1}$, while forecasts provide trajectories with a mean separation rate from OMA trajectories of 0.22 km $h^{-1}$.

When looking to the spatial distribution of inaccuracies in the forecast of trajectories, a good correspondence between the region of the highest forecast errors and those of less persistence can be observed. This has a straightforward interpretation: the method is learning more easily the most predictable patterns. What is interesting is that, in our study area, these regions are well defined and clear relationships can be established with the dynamical features identified in previous works, particularly those using HF radar data (e.g., Solabarrieta et al. 2014). The best skills are observed during winter, when persistence of current patterns is higher. Spatially, during winter the highest forecast errors are concentrated in the most energetic area, where the seasonal (and poleward) current is well established (Solabarrieta et al. 2014). During summer, when the current regime is much more variable (mostly linked to more variable winds and a less intense and persistent slope in the equatorward current), the persistence and forecast fields present much lower skills compared to the OMA fields. In both cases these are the lowest in the northwestern area, where the contribution of high-frequency (mostly inertial motions) processes can grow up to 40% of the total kinetic energy (see Fig. 8 in Solabarrieta et al. 2014). These results point to a possible way to improve the forecast by improving the learning strategy of the model. Instead of using a multiyear period of historical data, better results could be obtained by using seasonally conditioned learning periods or by separating the different contributions of the different physical processes (which have both different spatial and temporal variability scales) to the total variability before applying EOF decomposition (and thus forcing EOFs to split

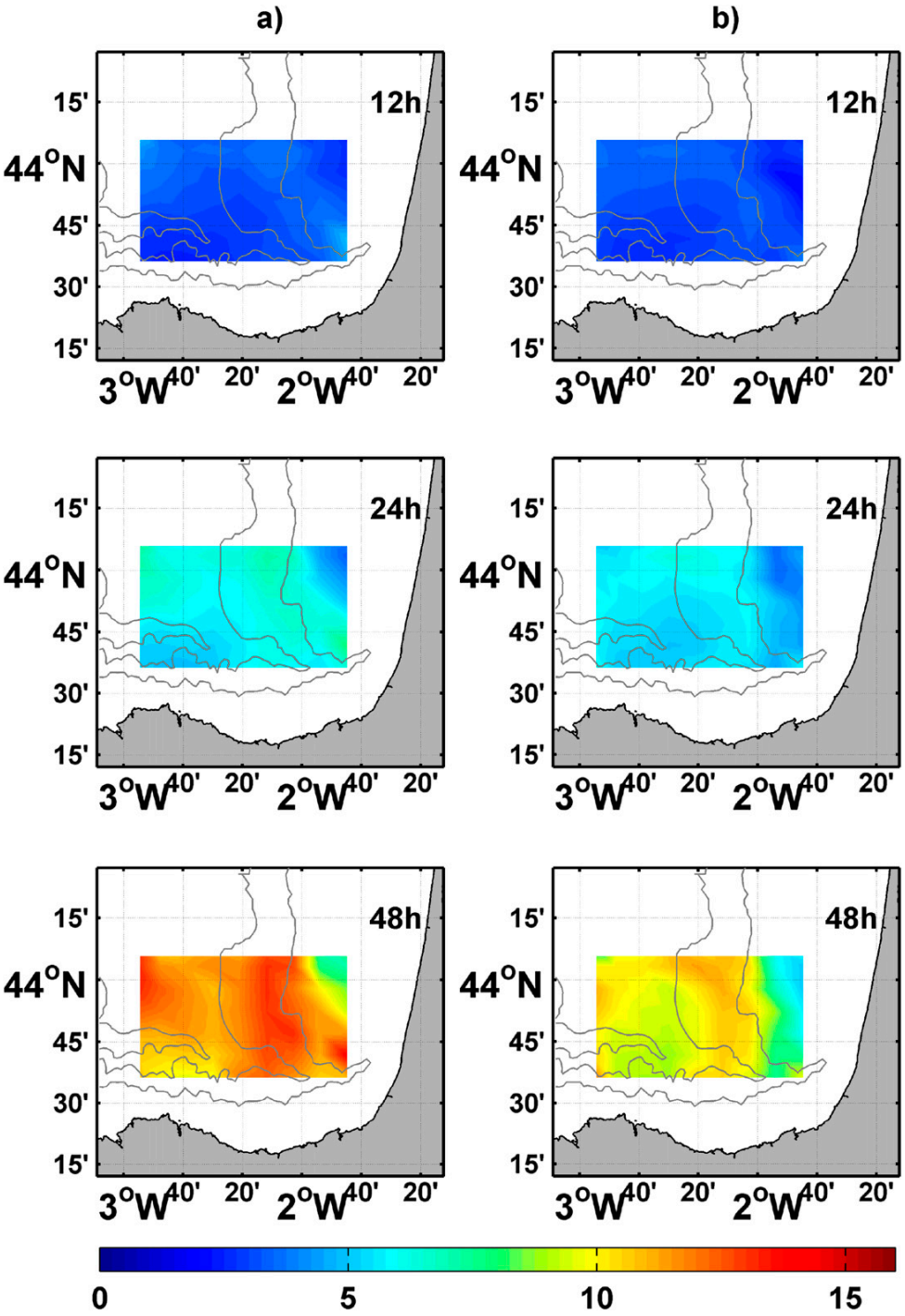


FIG. 7. Spatial distribution of errors (separation distance in km) in winter for (a) persistence and (b) forecast data products using trajectories from OMA currents as reference, in function of the initial position of the particle used for the computation of the trajectories.

correctly the different physical signals). Also, the use of HF radar data in combination with other datasets, like current fields derived from ocean forecast systems and forecast wind fields, could help improve forecast skills in the short term (after 12 hours of simulation). The benefits of using wind fields are discussed in Frolov et al. (2012).

Better results could also be expected for a higher-resolution dataset. The benefits of a long-range HF radar system reside in extended footprints, but the resolution in space is reduced. For some operational needs (i.e., search and rescue operations), higher-resolution fields could be more appropriate. New analyses using the data closer to the antennas, where refined grids for total velocities can be obtained due to a denser coverage of radials, are needed to evaluate further the possibility of improved forecasts. In any case, it has to be highlighted that for all the analyses performed, the forecast method is always equal to or better than the persistence fields and very similar to those of the total fields. This result confirms the utility of the forecast method for both short time lags and for wide forecast windows up to 48 hours for which the observed errors are under 15 km.

The results obtained in our experiments prove the adequacy of the HF radar used here to provide data for operational monitoring of the coastal areas. Indeed, the use of real-time HF radar data and derived products, such as the short-term forecast, has proven to have significant impact on the reduction of operational search radii in real situations (e.g., Roarty et al. 2010; Breivik et al. 2013). Other examples of the application of these data to different issues have been detailed in several publications (Paduan and Washburn 2013; Wyatt 2014). It is worth noting that the computational requirements to obtain forecast velocity fields are similar to those used to compute OMA velocity fields, so they could be generated operationally.

Finally, the high correlation observed between HF radar–derived surface currents and those along the water column shown in Solabarrieta et al. (2014) opens new research lines toward the estimation and forecast of 4D ocean transports using operational HF radar data in combination with other observations to provide information about the dynamics at deeper levels. The vertical coherence for surface patterns is expected to be seasonally modulated. Thus, again, careful choices of the data periods and analysis strategy should be made in view of the physical processes characterizing the local dynamics.

## 6. Conclusions

The skills to reproduce observed trajectories of real-time and forecast HF radar–derived products have been analyzed using a set of drifter data available in the radar footprint area in 2009. Then, the skills of the short-term forecast model (Frolov et al. 2012) used to obtain a forecast from hourly current fields are analyzed in terms of spatial and temporal distributions, for a longer time period. This paper provides quantitative evaluation of the capability of a coastal long-range HF radar data system to generate trajectories for real situations, with reasonable accuracy and low computational costs. Besides, the forecast model used here is proved to provide accurate forecast of real trajectories within an operational window of 48 hours. The benefits of the forecast methodology in absolute terms and with respect to the persistence fields are shown to be variable in time and space in relation to the modulation of the different physical processes governing the local ocean circulation. New approaches for improved forecasts are suggested in light of the obtained results and deserve further research.

*Acknowledgments.* The work of L. Solabarrieta in this study has been supported by the doctoral grant from Fundación Centros Tecnológicos Iñaki Goenaga. The work of A. Rubio and J. Mader was partially supported by the JERICO_NEXT project, funded by the European Commission's Horizon 2020 Programme (Contract 65 4410). The authors thank the Directorate of Emergency Attention and Meteorology of the Basque government for providing the radial HF radar data. The HF radar processing toolbox HFR_Progs was provided by D. Kaplan, M. Cook, D. Atwater, and J. F. Gonzlez. Finally, we also thank the sampling staff of the Marine Research Unit of AZTI-Tecnalia.

## REFERENCES

Barrick, D. E., 1977: Extraction of wave parameters from measured HF radar sea-echo Doppler spectra. *Radio Sci.*, **12**, 415–424, doi:10.1029/RS012i003p00415.

Benson, D. J., 1992: Computational methods in Lagrangian and Eulerian hydrocodes. *Comput. Methods Appl. Mech. Eng.*, **99**, 235–394, doi:10.1016/0045-7825(92)90042-I.

Berta, M., L. Bellomo, M. G. Magaldi, A. Griffa, A. Molcard, J. Marmain, M. Borghini, and V. Taillandier, 2014: Estimating Lagrangian transport blending drifters with HF radar data and models: Results from the TOSCA experiment in the Ligurian Current (North Western Mediterranean Sea). *Prog. Oceanogr.*, **128**, 15–29, doi:10.1016/j.pocean.2014.08.004.

Breivik, O., A. A. Allen, C. Maisondieu, and M. Olagnon, 2013: Advances in search and rescue at sea. *Ocean Dyn.*, **63**, 83–88, doi:10.1007/s10236-012-0581-1.

Charria, G., and Coauthors, 2013: Surface layer circulation derived from Lagrangian drifters in the Bay of Biscay. *J. Mar. Syst.*, **109–110** (Suppl.), S60–S76, doi:10.1016/j.jmarsys.2011.09.015.

Fernández, D. M., J. F. Vesecky, and C. C. Teague, 1996: Measurements of upper ocean surface current shear with

high-frequency radar. *J. Geophys. Res.*, **101**, 28 615–28 625, doi:10.1029/96JC03108.

Ferrer, L., A. Fontán, J. Mader, G. Chust, M. González, V. Valencia, A. Uriarte, and M. Collins, 2009: Low-salinity plumes in the oceanic region of the Basque Country. *Cont. Shelf Res.*, **29**, 970–984, doi:10.1016/j.csr.2008.12.014.

Fontán, A., and B. Cornuelle, 2015: Anisotropic response of surface circulation to wind forcing, as inferred from high-frequency radar currents in the southeastern Bay of Biscay. *J. Geophys. Res. Oceans*, **120**, 2945–2957, doi:10.1002/2014JC010671.

——, G. Esnaola, J. Sáenz, and M. González, 2013: Variability in the air–sea interaction patterns and timescales within the south-eastern Bay of Biscay, as observed by HF radar data. *Ocean Sci.*, **9**, 399–410, doi:10.5194/os-9-399-2013.

Frolov, S., J. Paduan, M. Cook, and J. Bellingham, 2012: Improved statistical prediction of surface currents based on historic HF-radar observations. *Ocean Dyn.*, **62**, 1111–1122, doi:10.1007/s10236-012-0553-5.

González, M., A. Uriarte, A. Fontán, J. Mader, and P. Gyssels, 2004: Marine dynamics. *Oceanography and Marine Environment of the Basque Country*, A. Borja and M. Collins, Eds., Elsevier Oceanography Series, Vol. 70, Elsevier, 133–157, doi:10.1016/S0422-9894(04)80044-8.

Gurgel, K.-W., 1994: Shipborne measurement of surface current fields by HF radar. *Onde Electr.*, **74**, 54–59.

Kaplan, D. M., and F. Lekien, 2007: Spatial interpolation and filtering of surface current data based on open-boundary modal analysis. *J. Geophys. Res.*, **112**, C12007, doi:10.1029/2006JC003984.

Kersalé, M., L. Marié, B. L. Cann, A. Serpette, C. Lathuilière, A. L. Boyer, A. Rubio, and P. Lazure, 2016: Poleward along-shore current pulses on the inner shelf of the Bay of Biscay. *Estuarine Coastal Shelf Sci.*, **179**, 155–171, doi:10.1016/j.ecss.2015.11.018.

Kohut, J., H. Roarty, E. Randall-Goodwin, S. Glenn, and C. Lichtenwalner, 2012: Evaluation of two algorithms for a network of coastal HF radars in the mid-Atlantic Bight. *Ocean Dyn.*, **62**, 953–968, doi:10.1007/s10236-012-0533-9.

Le Cann, B., 1990: Barotropic tidal dynamics of the Bay of Biscay shelf: Observations, numerical modelling and physical interpretation. *Cont. Shelf Res.*, **10**, 723–758, doi:10.1016/0278-4343(90)90008-A.

——, and A. Serpette, 2009: Intense warm and saline upper ocean inflow in the southern Bay of Biscay in autumn–winter 2006–2007. *Cont. Shelf Res.*, **29**, 1014–1025, doi:10.1016/j.csr.2008.11.015.

Lipa, B., and D. Barrick, 1983: Least-squares methods for the extraction of surface currents from CODAR crossed-loop data: Application at ARSLOE. *IEEE J. Oceanic Eng.*, **8**, 226–253, doi:10.1109/JOE.1983.1145578.

Ohlmann, C., P. White, L. Washburn, E. Terrill, B. Emery, and M. Otero, 2007: Interpretation of coastal HF radar–derived surface currents with high-resolution drifter data. *J. Atmos. Oceanic Technol.*, **24**, 666–680, doi:10.1175/JTECH1998.1.

Paduan, J. D., and L. K. Rosenfeld, 1996: Remotely sensed surface currents in Monterey Bay from shore-based HF radar (Coastal Ocean Dynamics Application Radar). *J. Geophys. Res.*, **101**, 20 669–20 686, doi:10.1029/96jc01663.

——, and H. C. Graber, 1997: Introduction to high-frequency radar: Reality and myth. *Oceanography*, **10** (2), 36–39, doi:10.5670/oceanog.1997.18.

——, and L. Washburn, 2013: High-frequency radar observations of ocean surface currents. *Annu. Rev. Mar. Sci.*, **5**, 115–136, doi:10.1146/annurev-marine-121211-172315.

Pingree, R. D., and B. Le Cann, 1990: Structure, strength and seasonality of the slope currents in the Bay of Biscay region. *J. Mar. Biol. Assoc.*, **70**, 857–885, doi:10.1017/S0025315400059117.

——, and ——, 1992a: Anticyclonic eddy X91 in the southern Bay of Biscay, May 1991 to February 1992. *J. Geophys. Res.*, **97**, 14 353–14 367, doi:10.1029/92JC01181.

——, and ——, 1992b: Three anticyclonic slope water oceanic eddies (SWODDIES) in the Southern Bay of Biscay in 1990. *Deep-Sea Res.*, **39A**, 1147–1175, doi:10.1016/0198-0149(92)90062-X.

Roarty, H., and Coauthors, 2010: Operation and application of a regional high-frequency radar network in the Mid-Atlantic Bight. *Mar. Technol. Soc. J.*, **44**, 133–145, doi:10.4031/MTSJ.44.6.5.

Rubio, A., G. Reverdin, A. Fontán, M. González, and J. Mader, 2011: Mapping near-inertial variability in the SE Bay of Biscay from HF radar data and two offshore moored buoys. *Geophys. Res. Lett.*, **38**, L19607, doi:10.1029/2011GL048783.

——, A. Fontán, P. Lazure, M. González, V. Valencia, L. Ferrer, J. Mader, and C. Hernández, 2013a: Seasonal to tidal variability of currents and temperature in waters of the continental slope, southeastern Bay of Biscay. *J. Mar. Syst.*, **109–110** (Suppl.), S121–S133, doi:10.1016/j.jmarsys.2012.01.004.

——, L. Solabarrieta, M. González, J. Mader, S. Castanedo, R. Medina, G. Charria, and J. Aranda, 2013b: Surface circulation and Lagrangian transport in the SE Bay of Biscay from HF radar data. *MTS/IEEE OCEANS—Bergen, 2013*, IEEE, 7 pp., doi:10.1109/OCEANS-Bergen.2013.6608039.

Schmidt, R., 1986: Multiple emitter location and signal parameter estimation. *IEEE Trans. Antennas Propag.*, **34**, 276–280, doi:10.1109/TAP.1986.1143830.

Solabarrieta, L., A. Rubio, S. Castanedo, R. Medina, G. Charria, and C. Hernández, 2014: Surface water circulation patterns in the southeastern Bay of Biscay: New evidences from HF radar data. *Cont. Shelf Res.*, **74**, 60–76, doi:10.1016/j.csr.2013.11.022.

——, ——, M. Cárdenas, S. Castanedo, G. Esnaola, F. J. Méndez, R. Medina, and L. Ferrer, 2015: Probabilistic relationships between wind and surface water circulation patterns in the SE Bay of Biscay. *Ocean Dyn.*, **65**, 1289–1303, doi:10.1007/s10236-015-0871-5.

Stewart, R., and J. Joy, 1974: HF radio measurements of surface currents. *Deep-Sea Res. Oceanogr. Abstr.*, **21**, 1039–1049, doi:10.1016/0011-7471(74)90066-7.

Ullman, D., J. O. Donnell, J. Kohut, T. Fake, and A. Allen, 2006: Trajectory prediction using HF radar surface currents: Monte Carlo simulations of prediction uncertainties. *J. Geophys. Res.*, **111**, C12005, doi:10.1029/2006JC003715.

van Aken, H. M., 2002: Surface currents in the Bay of Biscay as observed with drifters between 1995 and 1999. *Deep-Sea Res. I*, **49**, 1071–1086, doi:10.1016/S0967-0637(02)00017-1.

Wyatt, L., 2014: High frequency radar applications in coastal monitoring, planning and engineering. *Aust. J. Civ. Eng.*, **12**, 1–15, doi:10.7158/14488353.2014.11463992.